



Solar Orbiter's first Venus flyby

M. Volwerk, T. S. Horbury, L. D. Woodham, S. D. Bale, C. Simon Wedlund,
D. Schmid, R. C. Allen, V. Angelini, W. Baumjohann, L. Berger, et al.

► To cite this version:

M. Volwerk, T. S. Horbury, L. D. Woodham, S. D. Bale, C. Simon Wedlund, et al.. Solar Orbiter's first Venus flyby: MAG observations of structures and waves associated with the induced Venusian magnetosphere. *Astronomy and Astrophysics - A&A*, 2021, 656, pp.A11. 10.1051/0004-6361/202140910 . hal-03531358

HAL Id: hal-03531358

<https://hal.sorbonne-universite.fr/hal-03531358>


Submitted on 18 Jan 2022

HAL is a multi-disciplinary open access archive for the deposit and dissemination of scientific research documents, whether they are published or not. The documents may come from teaching and research institutions in France or abroad, or from public or private research centers.

L'archive ouverte pluridisciplinaire **HAL**, est destinée au dépôt et à la diffusion de documents scientifiques de niveau recherche, publiés ou non, émanant des établissements d'enseignement et de recherche français ou étrangers, des laboratoires publics ou privés.

Solar Orbiter's first Venus flyby

MAG observations of structures and waves associated with the induced Venusian magnetosphere

M. Volwerk¹ , T. S. Horbury², L. D. Woodham², S. D. Bale³, C. Simon Wedlund¹, D. Schmid¹, R. C. Allen⁴, V. Angelini², W. Baumjohann¹, L. Berger⁸, N. J. T. Edberg⁶, V. Evans², L. Z. Hadid⁵, G. C. Ho⁴, Yu. V. Khotyaintsev⁶, W. Magnes¹, M. Maksimovic⁵, H. O'Brien², M. B. Steller¹, J. Rodriguez-Pacheco⁷, and R. F. Wimmer-Scheingruber⁸

¹ Space Research Institute, Austrian Academy of Sciences, Graz, Austria
e-mail: martin.volwerk@oeaw.ac.at

² Department of Physics, The Blackett Laboratory, Imperial College London, London, UK

³ Space Sciences Laboratory, University of California, Berkeley, CA, USA

⁴ The Johns Hopkins University, Applied Physics Laboratory, Laurel, MD, USA

⁵ LPP, CNRS, École Polytechnique, Sorbonne Université, Observatoire de Paris, Université Paris-Saclay, PSL Research University, Palaiseau, Paris, France

⁶ Swedish Institute of Space Physics (IRFU), Uppsala, Sweden

⁷ Universidad de Alcalá, Space Research Group, Alcalá de Henares, Spain

⁸ Institut für Experimentelle und Angewandte Physik, Christian-Albrechts-Universität zu Kiel, Kiel, Germany

Received 29 March 2021 / Accepted 11 May 2021

ABSTRACT

Context. The induced magnetosphere of Venus is caused by the interaction of the solar wind and embedded interplanetary magnetic field with the exosphere and ionosphere of Venus. Solar Orbiter entered Venus's magnetotail far downstream, >70 Venus radii, of the planet and exited the magnetosphere over the north pole. This offered a unique view of the system over distances that had only been flown through before by three other missions, Mariner 10, Galileo, and BepiColombo.

Aims. In this study, we study the large-scale structure and activity of the induced magnetosphere as well as the high-frequency plasma waves both in the magnetosphere and in a limited region upstream of the planet where interaction with Venus's exosphere is expected.

Methods. The large-scale structure of the magnetosphere was studied with low-pass filtered data and identified events are investigated with a minimum variance analysis as well as combined with plasma data. The high-frequency plasma waves were studied with spectral analysis.

Results. We find that Venus's magnetotail is very active during the Solar Orbiter flyby. Structures such as flux ropes and reconnection sites were encountered, in addition to a strong overdapping of the magnetic field downstream of the bow shock and planet. High-frequency plasma waves (up to six times the local proton cyclotron frequency) are observed in the magnetotail, which are identified as Doppler-shifted proton cyclotron waves, whereas in the upstream solar wind, these waves appear just below the proton cyclotron frequency (as expected) but are very patchy. The bow shock is quasi-perpendicular, however, expected mirror mode activity is not found directly behind it; instead, there is strong cyclotron wave power. This is most likely caused by the relatively low plasma- β behind the bow shock. Much further downstream, magnetic hole or mirror mode structures are identified in the magnetosheath.

Key words. planets and satellites: magnetic fields – plasmas – magnetic fields

1. Introduction

The interaction of the solar wind with the exosphere and ionosphere of Venus has given rise to the creation of a so-called induced magnetosphere (see e.g., [Luhmann 1986](#); [Phillips & McComas 1991](#); [Bertucci et al. 2011](#); [Dubinin et al. 2011](#); [Futaana et al. 2017](#)). Mass-loading of the solar wind through the ionisation of exospheric neutrals slows it down and leads to the creation of a bow shock; behind it, the super-magnetosonic solar wind is braked to sub-magnetosonic speeds. The interplanetary magnetic field (IMF) is convected towards the planet and magnetic flux builds up on the sub-solar side (e.g., [Zhang et al. 2008a](#)). Further away from the planet, the IMF is transported by the solar wind velocity and gets draped around

the planet leading to the creation of an induced magnetosphere (see e.g., [Saunders & Russell 1986](#)).

Downstream from the planet, a magnetotail is created, which consists of two lobes with oppositely directed magnetic fields, separated by a current sheet (e.g., [Phillips & McComas 1991](#)). Between these two lobes of stretched-out magnetic field and the bow shock exists the magnetosheath, where the slowed-down plasma gets accelerated back again to the pre-shocked solar wind velocity. However, as Venus has no intrinsic magnetic field ([Van Allen et al. 1967](#); [Russell et al. 1981](#); [Phillips & Russell 1987](#)), the normal to the current sheet is only dependent on the upstream IMF direction as a consequence of field line draping, rather than having a preferred direction in a planet based inertial frame. Just as in the case of the Earth's magnetotail, this structure

shows a wide range of activity, with: magnetic reconnection having been observed (Volwerk et al. 2009, 2010; Zhang et al. 2010) as well as magnetotail flapping (Vörös et al. 2008b; Rong et al. 2015). There is also a difference between the turbulent wave power in the magnetosheath compared to the lobes (Russell et al. 1981; Vörös et al. 2008a).

The first flythrough of Venus’s magnetotail was done by Mariner 10 (Lepping & Behannon 1978), from as far downstream as $\sim 100 R_V$ ($1 R_V \approx 6,051.8$ km, Venus radius). Other previous investigations of the magnetotail of Venus have been performed mainly using data from the Pioneer Venus Orbiter and Venus Express. However, their limited apoapsis meant that they were not able to study Venus’s magnetotail region further downstream than $\sim 11 R_V$. This means that there is still much to learn about the structure and behaviour of the magnetotail at further distances downstream of Venus. Questions such as how far the Venusian tail is extended downstream of the planet, how prone it is to magnetic reconnection events and at which locations, and to what extent it is influenced by the solar wind remain open. Recently, several new missions have been launched, using Venus for gravity assists in order to reach their final orbit or goal. We consider whether these missions provide the opportunity to gain further insights into the dynamics of the Venusian magnetosphere.

The Parker Solar Probe (Fox et al. 2016) has a total of seven Venus flybys to adjust the spacecraft’s orbit for closer perihelia during solar encounters. Two flybys on 3 October 2018 and 26 December 2019, approaching Venus from downstream, showed strong kinetic-scale turbulence in the magnetosheath (Bowen et al. 2021), sub-proton scale magnetic holes (Goodrich et al. 2021), and double layers near the bow shock (Malaspina et al. 2020).

BepiColombo, ESA’s mission to Mercury (Anselmi & Scoon 2001; Benkhoff et al. 2010), has used two Venus flybys in order to brake enough to reach and insert the spacecraft into orbit around the innermost planet. The first flyby took place on 15 October 2020, approaching Venus from the upstream direction and leaving the neighbourhood of the planet via a long passage through the magnetotail. During this flyby, evidence was found of draping in the magnetosheath in the direction perpendicular to the Venus-Sun line (Volwerk et al. 2021), by field lines hanging up at Venus’s pile-up boundary on one side and being connected to the solar wind at the other, confirming previous finding with Venus Express (Delva et al. 2017). Further down the tail, near the centre, close to the central plasma sheet-current sheet, flapping was observed. The second flyby will occur on 11 August 2021, only two days after Solar Orbiter carries out its second Venus flyby.

Solar Orbiter (Müller et al. 2013, 2020), the mission that is the focus of this paper, will have a total of seven Venus gravity assist manoeuvres to end up in a highly inclined orbit, at $\sim 33.4^\circ$, around the Sun with a 2:3-resonance with Venus’s orbit after the seventh flyby in June 2029. The second Venus flyby will be in August 2021, two days before BepiColombo will have its second flyby of Venus. The third flyby will be in the third quarter of 2022.

2. Data

We use the Solar Orbiter high-resolution (8 Hz, normal mode) magnetometer data (Horbury et al. 2020) of the first Venus flyby on 27 December 2020 to study the induced magnetosphere and the plasma wave activity around Venus. The spacecraft approached the planet from downstream, through the induced magnetotail and left the induced magnetosphere over Venus’s

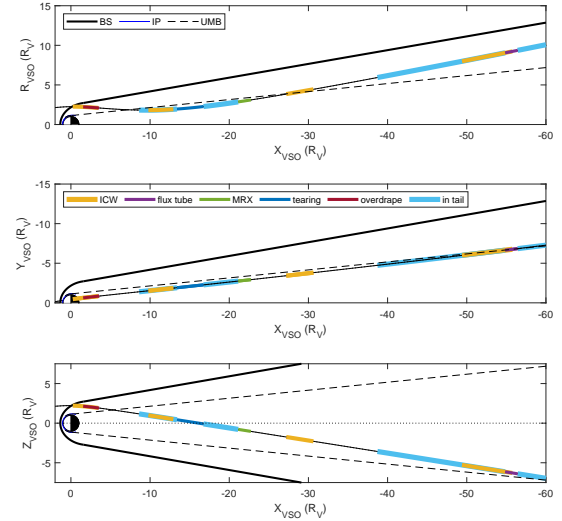


Fig. 1. Visualisation of the first Venus flyby by Solar Orbiter and in cylindrical VSO coordinates (*top panel*), in the $X - Y$ -(*middle panel*), and $X - Z$ -planes (*bottom panel*). Shown: Bow shock (BS), ionopause (IP) and upper mantle boundary (UMB); see legend in top panel, as well as the regions where Solar Orbiter was in the magnetosheath and where different wave activity was detected (see legend in the middle panel).

north pole before finally passing through the bow shock. The closest approach to the planet was at $\sim 2.26 R_V$ from the centre of the planet at $\sim 12:40$ UT. The flyby geometry is shown in Fig. 1, where also the location of different activity in the induced magnetotail is colour-coded, as well as the locations where the spacecraft is suspected to be in the magnetosheath. We used the bow shock and ionopause model from Zhang et al. (2008b) and the Martinecz et al. (2009a) upper mantle boundary model (see also, Martinecz et al. 2009b, for a correction). The data are shown in Fig. 2 in the Venus Solar Orbital (VSO) coordinate system, where X_{VSO} is along the Venus-Sun line, Y_{VSO} is in the opposite direction of Venus’s orbital velocity, and Z_{VSO} completes the triad, in the direction of Venus’s rotational axis. Also, the same colour-coding as in Fig. 1 is used here. Unless otherwise specified, the data are in VSO coordinates. Figure 3 shows a 3D rendering of the magnetic field along the orbit of Solar Orbiter.

To support the magnetometer data, we also used the measurements from the Energetic Particle Detector – Supra Thermal Electrons and Protons instrument (EPD-STEP; Rodríguez-Pacheco et al. 2020), showing energetic ions as well as Radio and Plasma Waves (RPW; Maksimovic et al. 1986) observations of the electron density determined from quasi-thermal noise (QTN; i.e. the plasma frequency) and the Space-Craft Potential (SCP; Khotyaintsev et al. 2021; Hadid et al. 2021).

3. Large structure of induced magnetosphere

In order to study the large-scale structure of the induced magnetosphere, the data are low-pass filtered, with a cut-off frequency of $1/300$ Hz (5 min); the cone (θ_c) and clock (ϕ_c) angles of the magnetic field are calculated as follows:

$$\theta_c = \tan^{-1} \left(\frac{\sqrt{B_y^2 + B_z^2}}{B_x} \right), \quad (1)$$

$$\phi_c = \tan^{-1} \left(\frac{B_z}{B_y} \right). \quad (2)$$

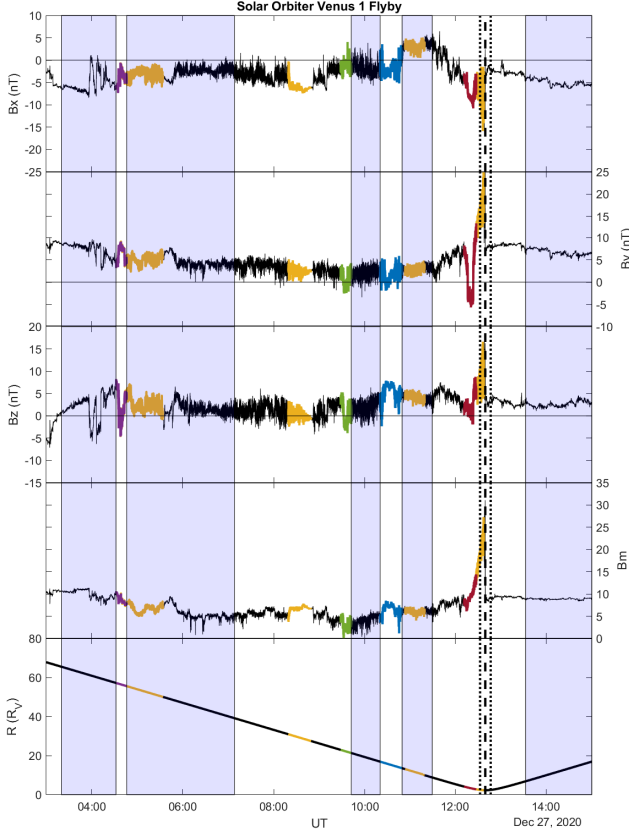


Fig. 2. Magnetometer data, all three components and magnitude and the radial distance from Venus in VSO coordinates. The dashed vertical line is the time of the bow shock crossing, the dotted vertical lines show the region $\pm 1 R_V$. The blue shaded intervals indicate where the field has the direction of the upstream solar wind. The colouring of the traces is according to which activity is observed in the magnetic field, as in Fig. 1.

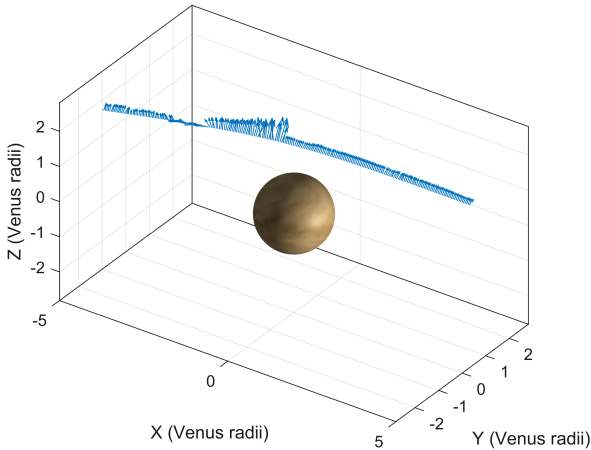


Fig. 3. 3D view of the Venus flyby, with the magnetic field vectors plotted along the orbit of Solar Orbiter crossing over Venus's north pole.

A cone angle of $\theta_c = 0^\circ(180^\circ)$ implies a sunward (anti-sunward) directed B -field and $\theta_c = 90^\circ$ a field directed perpendicular to the Venus-Sun line. The clock angle ϕ_c is the direction in the YZ_{VSO} -plane with $\phi_c = 0^\circ$ indicating an eastward pointing field and $\phi_c = 90^\circ$ a northward one. The result is shown in Fig. 4.

First of all, we observe that the cone angle in the solar wind in the interval between 10:30–15:00 UT, $\theta_{c,SW} \approx 120^\circ$, namely,

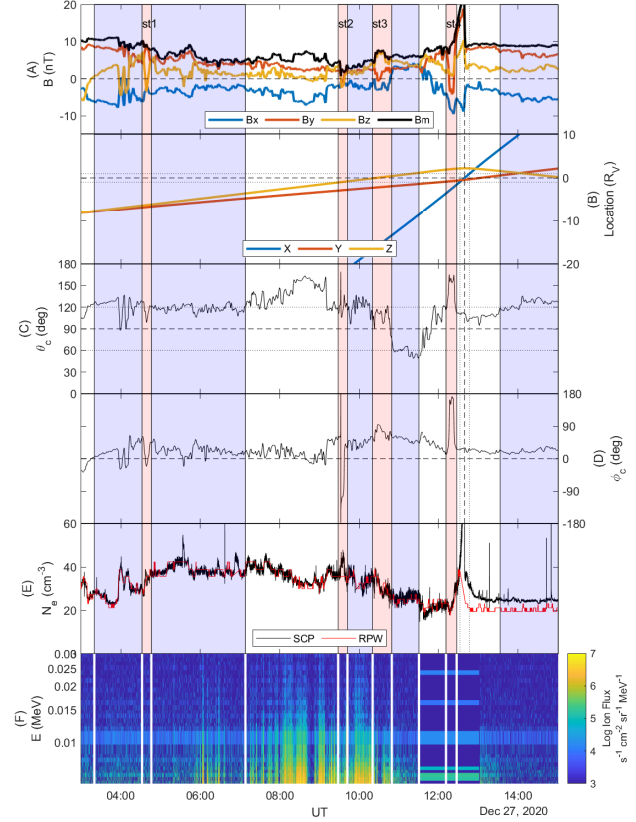


Fig. 4. Combined instrument data for the ~ 12 h flyby through the induced magnetotail and into the solar wind. (A) Low-pass filtered magnetic field data; (B) Location of the spacecraft in R_V ; (C) The cone angle θ_c ; (D) The clock angle ϕ_c ; (E) The electron density determined from RPW (red) and SCP (black); (F) The time-energy spectrogram of the EPD-STEP instrument. The blue-shaded intervals indicate where the field has the direction of the upstream solar wind. The red-shaded intervals indicate significant structures in the magnetic field. The two dotted lines in the cone angle panel C at $\theta_c = 60^\circ/120^\circ$ show the solar wind $\theta_{c,SW} \approx 120^\circ$. The vertical black dashed and dotted lines show $X_{VSO} = 1$ and $\pm 1 R_V$, respectively.

anti-sunward, a direction which is also seen in the downstream region of Venus, up to $\sim 08:00$ UT, when the spacecraft was $\sim 33 R_V$ away from the planet. The nominal Parker spiral angle at Venus is $\theta_p \approx 36^\circ/144^\circ$, so the field is slightly less radial than nominal. The downstream regions where the cone angle is almost the same as the upstream solar wind cone angle are shaded in blue in Figs. 2 and 4.

After $\sim 08:00$ UT, θ_c increases to $\sim 160^\circ$, indicating a more draped and tail-like, magnetic field, that is, the field is in more aligned with the Venus-Sun line as compared to the solar wind. This is the case up until $\sim 09:10$ UT when the field turns back to the background, solar wind state. At $\sim 10:45$ UT the field turns sunward at $\theta_c \approx 60^\circ$ until $\sim 11:30$ UT, which is the solar wind direction with the oppositely directed field.

At a distance of $\sim 8.5 R_V$, at $\sim 11:30$ UT, Solar Orbiter enters the region that is most influenced by the interaction of the solar wind with Venus. The magnetic field magnitude starts to increase, which is also seen in all three components. There is an interesting structure in both B_y and B_z at $\sim 12:20$ UT, showing a strong rotation in the field, with B_y changing sign.

Overall, the clock angle remains near $\phi_c \approx 20^\circ$ (eastward) until $\sim 09:10$ UT, where it increases to $\phi_c \approx 60^\circ$ (more northward), then slowly decreases again to the solar wind value $\phi_c \approx 20^\circ$;

Table 1. Eigenvalues, λ , and eigenvectors for the MVA analysis on the four red-shaded magnetic structures and the bow shock, as well as the central time and location.

	λ	Eigenvector	Time (UT)	Loc. (R_V)
st1	0.08	(0.59, 0.61, 0.53)	04:32–04:46	(-55, -6, -6)
	0.29	(0.74, -0.67, -0.04)		
	15.0	(-0.34, -0.41, 0.85)		
st2	0.07	(0.58, 0.61, 0.53)	09:28–09:42	(-21, -3, -1)
	0.26	(0.74, -0.67, -0.04)		
	5.98	(-0.34, -0.41, 0.85)		
st3	0.31	(0.22, -0.81, -0.54)	10:20–10:49	(-15, -2, 0)
	1.11	(-0.85, 0.09, -0.51)		
	31.7	(-0.47, -0.57, 0.67)		
st4	0.14	(-0.67, 0.36, -0.64)	12:12–12:28	(-3, -1, 2)
	2.23	(-0.70, -0.02, 0.72)		
	31.8	(0.25, 0.93, 0.27)		
BS	1.15	(-0.40, 0.31, -0.86)	12:39:30–12:40:15	(0.0, -0.4, 2.2)
	2.07	(0.83, 0.51, -0.20)		
	71.0	(-0.37, 0.80, 0.46)		

this is valid except for the $B_x - B_z$ structure, where the clock angle increases to $\phi_c \approx 70^\circ$ (westward).

Before discussing these structures in more detail, we present some observations of the upstream solar wind for context. As can be seen in Fig. 4 in the last blue box, upstream of the bow shock, the average magnetic field vector is $\mathbf{B} \approx [-5, 6, 3]$ nT. This field direction has consequences for the draping of the magnetic field around the planet, such that the symmetry plane for the draped field (and thus the induced tail) is tilted in the $Y - Z$ -plane by $\sim 15-30^\circ$ (see the clock angle ϕ_c).

Marked structures (st1 through st4, discussed below) have been identified by eye using the low-pass filtered magnetic field data and the cone and clock angle. They also stand out by their strong variations in magnetic field strength. Combining the presence of these structures, which are mainly typical structures found in the magnetotail proper, being outside of where the field has the solar wind cone angle, is an indication that the blue boxes demonstrate when the spacecraft is in the magnetosheath.

3.1. Marked structures

Marked magnetic structures are highlighted in red in Fig. 4 and studied below. We performed a minimum variance analysis (MVA, Sonnerup & Scheible 1998) on the data and transformed them to MVA coordinates. The results of the MVA analysis for each red-shaded interval are shown in Table 1.

3.1.1. st1: flux tube

The first magnetic structure, st1, at $\sim 04:40$ UT and $\sim (-55, -6, -6)R_V$ shows a slightly decreasing field magnitude, $B_m = 10 \rightarrow 7$ nT, and a strong rotation in $B_{\max} = 7 \rightarrow -6 \rightarrow 3$ nT. This may be consistent with the passage of a plasmoid/flux rope. The minimum variance direction, given in Table 1 shows that the axis is significantly tilted with respect to the tail axis. Figure 5 shows a zoom-in on this interval, with the magnetic field data in both VSO and MVA coordinates.

Interestingly, there seem to be three jumps in the electron density as measured from the spacecraft potential, indicated by the vertical dotted lines. The resolution of the QTN data is not high enough to capture this structure in the density, but overall,

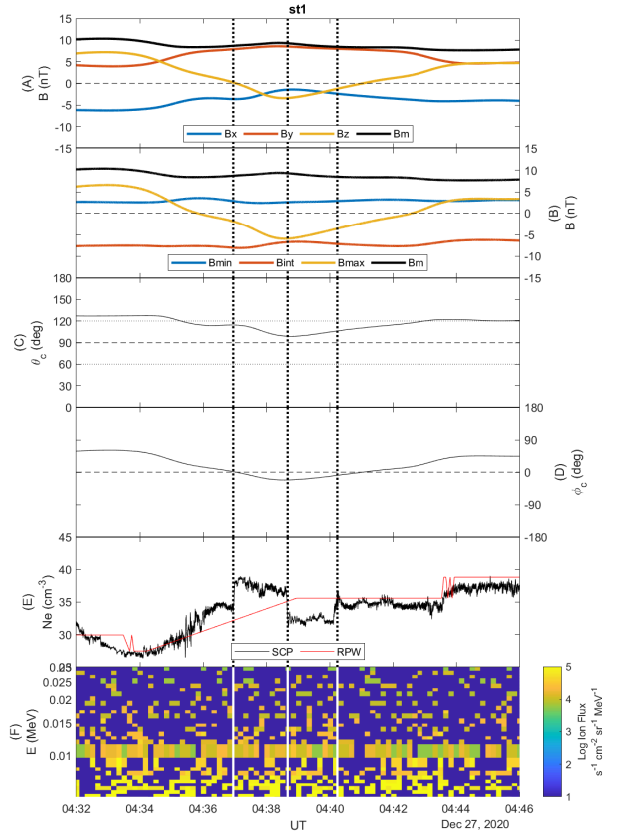


Fig. 5. Zoom-in on the flux tube: st1. Shown: (A) Magnetic field data in VSO coordinates; (B) The magnetic field in MVA-coordinates; (C) The cone angle θ_c ; (D) The clock angle ϕ_c ; (E) The electron density determined from RPW (red) and SCP (black); (F) The time-energy spectrogram of the EPD-STEP instrument. The three dotted vertical lines show where B_z changes sign and has its minimum negative value. The horizontal line at 0.01 MeV in panel F is an instrumental artefact.

the two datasets agree quite nicely. These are close to where B_z changes signs (first and last) and B_z reaches a minimum negative value. However, the electron density increases throughout this structure, as can also be seen in Fig. 4.

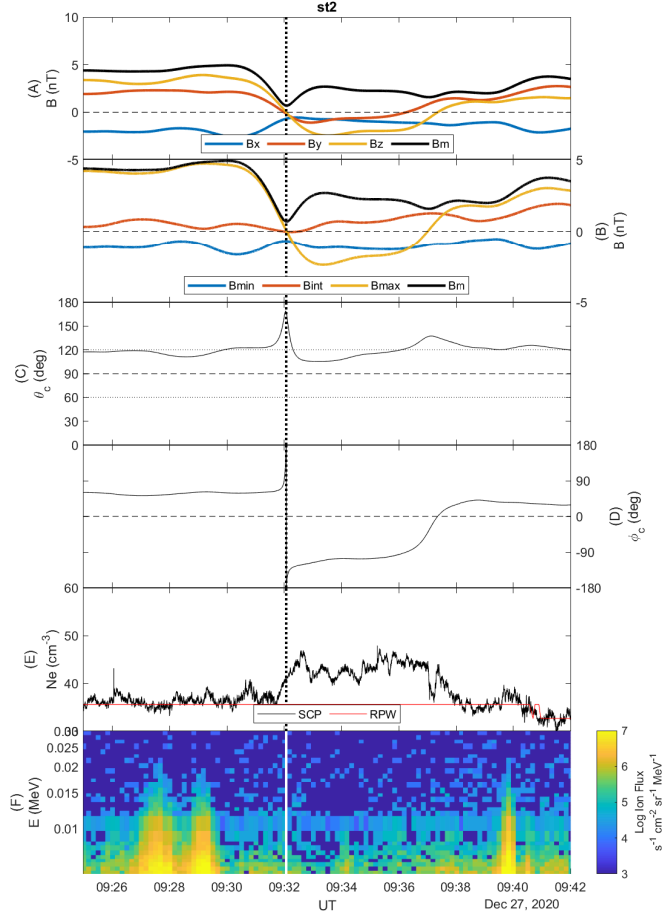


Fig. 6. Zoom-in on the magnetic reconnection event: st2. Same format as Fig. 5.

3.1.2. st2: reconnection site

The second structure, st2, displayed in the zoom-in in Fig. 6, at $\sim 09:34$ UT and $\sim (-21, -3, -1) R_V$ shows a strong decrease in the magnitude of the field $B_m = 4.5 \rightarrow 0.7$ nT, which might be indicative of Solar Orbiter crossing a magnetic reconnection site (see e.g., Volwerk et al. 2009, 2010). Looking again in VSO coordinates, we find that B_x remains negative and both B_y and B_z change signs. In MVA coordinates we clearly see how the maximum variance component change sign, with the other two components decreasing slightly near the minimum in B_m .

The EPD/STEP data in the bottom panel show a population of ions at $\lesssim 7$ keV before the crossing. After the crossing there are significantly less counts. The viewing direction of EPD/STEP is roughly sunward, which is consistent with the observation of energised ions before crossing the reconnection site, where the ions are tailward accelerated towards the instrument aperture.

The electron density from the spacecraft potential shows clearly two different regions on either side of the reconnection site. The Venus-ward side of the reconnection site shows an increase of $\Delta N_e \approx 10 \text{ cm}^{-3}$, which decreases again later at $\sim 09:38$ UT, when B_{\max} reverses sign again. The spacecraft most likely exits the region of reconnected field lines at this point, with all three magnetic field components returning to their pre-event values. The two peaks in the STEP spectrogram around $\sim 09:28$ UT can be related to Solar Orbiter crossing the separatrix, along which accelerated ions are travelling towards the detector.

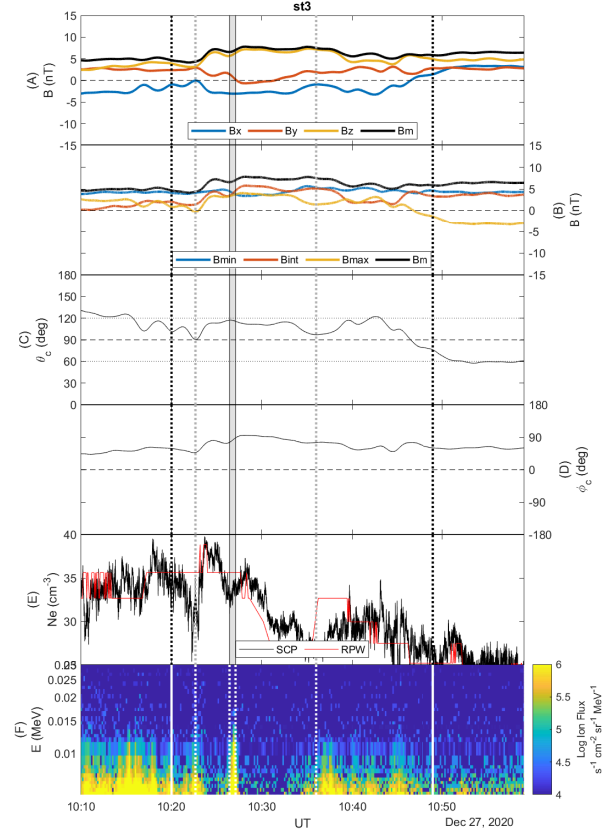


Fig. 7. Zoom-in on the tearing instability region: st3; shown in the same format as in Fig. 5. The two grey dotted lines show where the cone angle $\theta_c \approx 90^\circ$. The grey-shaded area shows where EPD-STEP shows a burst of energetic ions.

3.1.3. st3: tearing instability

Structure st3, displayed in the zoom-in in Fig. 7, around $\sim 10:30$ UT and $\sim (-15, -2, 0) R_V$ shows an interesting behaviour. Around the first black dotted line there are three depressions in B_x where the cone angle $\theta_c \rightarrow 90^\circ$. During the steady decrease of B_x over these three depressions, B_z increases slightly, whereas B_y remains constant. With the very steep θ_c , this is reminiscent of magnetotail dipolarisations in the Earth's magnetotail, with little variation in the total magnetic field strength B_m (see e.g., Schmid et al. 2011).

After the last dipolarisation, the first grey dotted line, the magnetic field strength starts to increase through an increase in B_x and B_z combined with a slightly decreasing B_y . This leads to a rotation of the clock-angle back to a more tail-like value, $\phi_c \approx 120^\circ$. The field remains relatively stable until the second grey dotted line, where B_x again decreases, with a slight increase in B_y , and the cone angle decreases again to $\theta_c \approx 97^\circ$. Towards the end of the structure, the cone angle changes from $\theta_c \approx 120^\circ$ to $\sim 60^\circ$, namely, in the complementary direction.

The (near) cross-tail direction of the magnetic field, $\theta_c \approx 90^\circ$, may be an indication that the spacecraft is passing through the neighbourhood of possible reconnection sites, where closed field lines might exist. The first and second grey dotted lines, with both near-northward field indicate that this might be a region of 'closed field lines'. The EPD-STEP data in panel (E) show that between these two lines, the energetic ions disappear, except for a burst at the grey-shaded area, which occurs when B_y changes sign and there is a small decrease in B_m .

The electron density increases strongly after the last dipolarisation, and decreases towards the grey-shaded area (back to almost pre-event value) and then decreases further. This indicates that there are two regions inside this structure, separated by the burst in the EPD-STEP data and B_y changing sign.

The whole structure, bounded by two dipolarised field regions, can be explained with a tearing instability (see e.g., [Treumann & Baumjohann 1996](#)) acting in Venus's magnetotail, creating two or more X-lines with O-lines in between. Because of the sign-change of B_y , the differences in the electron density and the strong burst in EPD-STEP it could be argued that Solar Orbiter is passing by a separatrix, moving from one magnetic island to another, without actually seeing the X-line in between.

3.1.4. st4: over-draping

The last structure, st4, displayed as a zoom-in in Fig. 8, is just downstream of Venus right before crossing the bow shock, where there is a strong rotation in the magnetic field, mainly in B_y but also evident in B_z , see Fig. 8. Apart from the gradual decrease behind the bow shock, the magnitude of the magnetic field does not change, indicating it is a true rotation of the field. At the boundaries of this rotation, there are small decreases in B_m , created by the currents facilitating the rotation of the field.

This structure is reminiscent of an 'over-draping' of the field (see e.g., [Zhang et al. 2010](#); [Dubinin et al. 2013](#); [Futaana et al. 2017](#)). The magnetic field in the magnetosheath is influenced by the ionospheric magnetic field, induced by ionospheric currents, and as a result, the field lines wrap around the planet. This effect can be so strong that the field drapes too far around Venus, such that the B_y and B_z components change signs (or in this case $B_z \rightarrow 0$).

3.2. Bow shock

The bow shock crossing occurs around $\sim 12:40$ UT at $\sim (0.02, -0.43, 2.22) R_V$ from the centre of the planet. Figure 9 shows a zoom-in on this interval, with the magnetic field data in VSO (top) and MVA (bottom) coordinates. Because of the large magnetic fluctuations on the bow shock ramp, the MVA is not well determined, as can be seen in Table 1, with $\lambda_{\min} \sim \lambda_{\text{int}} \ll \lambda_{\max}$. The shock normal direction would result in an angle between normal and upstream magnetic field of $\angle(\mathbf{B}, \mathbf{n}_{\text{MVA}}) \approx 68^\circ$. A better estimate for the normal may be obtained by the magnetic coplanarity method given by ([Schwartz 1998](#)):

$$\mathbf{n}_{\text{mc}} = \pm \frac{(\mathbf{B}_d \times \mathbf{B}_u) \times \Delta \mathbf{B}}{|(\mathbf{B}_d \times \mathbf{B}_u) \times \Delta \mathbf{B}|}, \quad (3)$$

$$\Delta \mathbf{B} = \mathbf{B}_d - \mathbf{B}_u, \quad (4)$$

where \mathbf{B}_d and \mathbf{B}_u are the downstream (12:39:40–12:39:46 UT) and upstream (12:39:54–12:40:00 UT) magnetic field vectors, respectively. This results in a normal direction $\mathbf{n}_{\text{mc}} = \pm(0.48, 0.61, -0.63)$, which results in an angle between normal and upstream magnetic field of $\angle(\mathbf{B}, \mathbf{n}_{\text{mc}}) \approx 88^\circ$, indicating a quasi-perpendicular bow shock.

There are strong oscillations on the ramp of the bow shock, which are elliptically right-hand polarised in the $(B_{\text{max}}, B_{\text{int}})$ -plane. The middle panel of Fig. 9 shows that the electron density variation is in phase with the magnetic field strength variation, consistent with fast-mode and magnetosonic type oscillations (see e.g., [Allen et al. 2021](#); [Dimmock et al. 2021](#)).

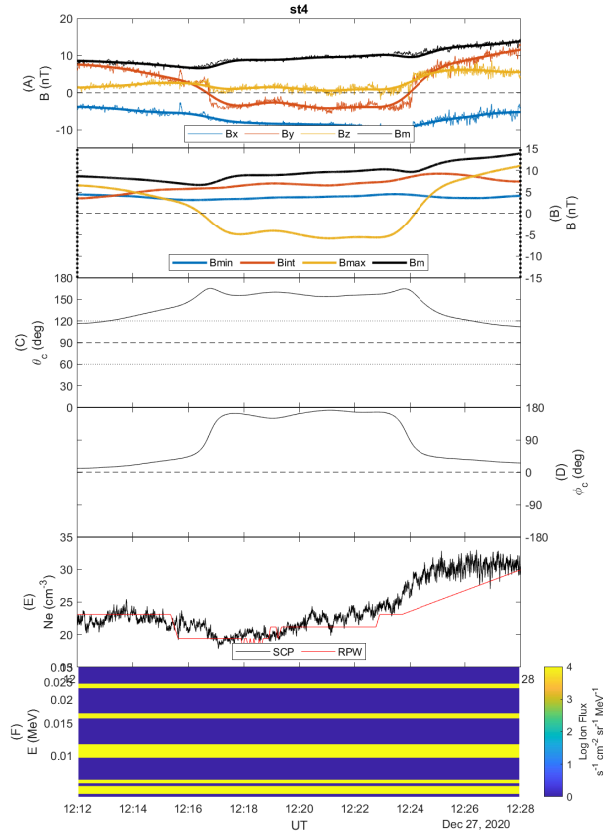


Fig. 8. Zoom-in on the overdapping: st4; shown in the same format as in Fig. 7. We note that the EPD-STEP instrument was in a non-operational mode during this period.

4. High-frequency magnetic fluctuations

The interaction of the solar wind with Venus's exosphere and ionosphere gives rise to large-scale MHD phenomena as discussed above, and also micro-scale and kinetic effects such as ion pick-up and acceleration. High-frequency, in this context, should be interpreted as waves with frequencies up to ten times the proton gyro frequency. Venus has been shown to have a large hydrogen exosphere that expands well beyond the bow shock ([Delva et al. 2009](#)). Photo-ionisation of the neutral hydrogen atoms leads to proton pick-up in the solar wind. These new ions create a ring-beam distribution which is prone to the growth of two unstable modes: the ion cyclotron (IC) and the mirror mode (MM) instabilities ([Gary 1992](#)). Which of the two instabilities will grow is dependent on the plasma- β (the ratio between plasma and magnetic pressure). For small β , for instance, in the solar wind, the IC instability dominates ([Hellinger et al. 2006](#); [Matteini et al. 2007](#); [Bale et al. 2009](#); [Woodham et al. 2018, 2019](#)), whereas for high β , for instance, behind the bow shock, the MM instability plays a major role ([Volwerk et al. 2008a,b, 2016](#); [Fränz et al. 2017](#); [Bader et al. 2019](#)).

4.1. Ion cyclotron waves

Local ion pick-up in the solar wind creates a ring-beam distribution, which may generate IC waves that will be observed as left-hand polarised waves below the local cyclotron frequency in the spacecraft frame through the anomalous Doppler shift (see e.g., the discussions in [Mazelle & Neubauer 1993](#); [Delva et al. 2008](#)). However, 'elsewhere', non-locally generated IC waves,

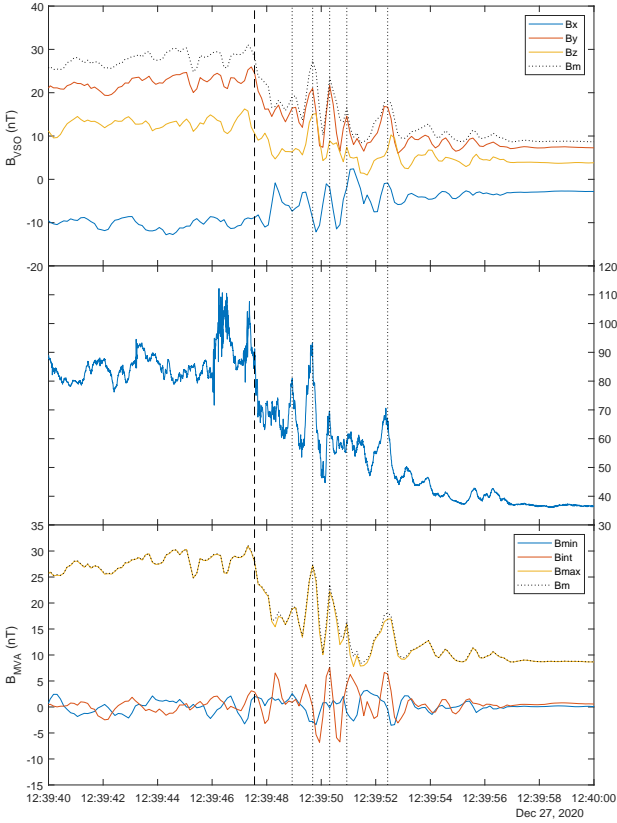


Fig. 9. Venus's bow shock in VSO (*top*) and MFA (*bottom*) coordinates with the electron density in the *middle panel*. The dotted vertical lines show the alignment of the peaks in B_m and B_{max} and N_e on the bow shock ramp.

subsequently transported by the solar wind, will be observed as Doppler-shifted waves, and may, thereby, change handedness (e.g., Woodham et al. 2019).

In order to study these waves, the magnetic field data are transformed to a mean-field aligned (MFA) coordinate system, where Z_{MFA} is along the low-pass filtered magnetic field and X_{MFA} and Y_{MFA} are combined into a right- and left-handed coordinate:

$$R = (X_{MFA} + iY_{MFA})/2, \quad (5)$$

$$L = (X_{MFA} - iY_{MFA})/2. \quad (6)$$

A dynamical spectrum is produced by calculating the power spectral density (PSD) in overlapping windows of 1024 points (128 s) shifted over 64 points (8 s). The result for the compressional (C , which is the Z_{MFA} -component) and left- and right-handed polarised fields are shown in Fig. 10. The local proton cyclotron frequency is shown by the thin white line in each panel.

4.1.1. Magnetosheath

In all three dynamic spectra of the C , R , and L components there is broad-band power below f_{cp} . However, the L component shows enhanced spectral power above f_{cp} compared to R and C . In order to further investigate the ratio between the PSD of both components $D = L/R$ is calculated, which is shown in the bottom panel of Fig. 10. There are patches with strong left-hand polarised wave power. The frequency variation of these signatures is highly correlated with f_{cp} , but shifted to higher

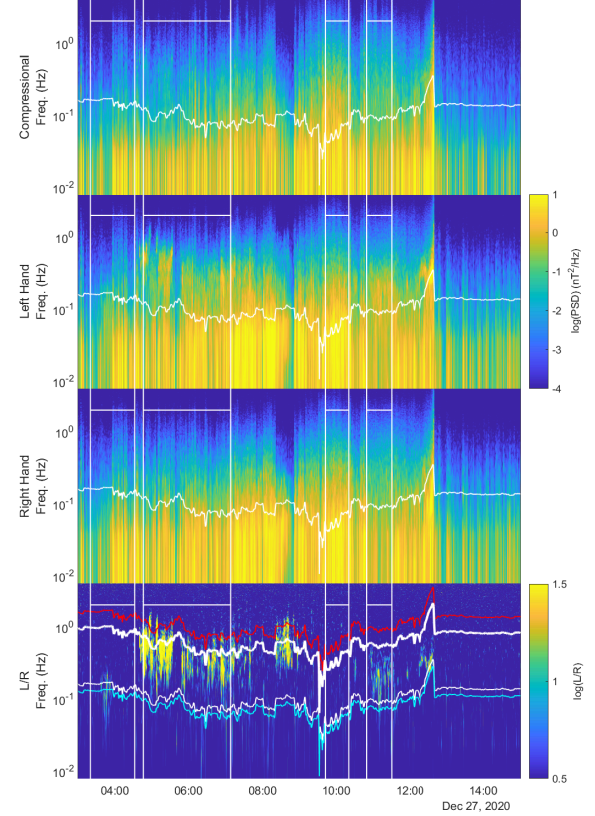


Fig. 10. Dynamical spectra of the compressional (C), left- (L), and right-hand (R) polarised field components during the entire flyby. The white vertical lines connected by horizontal lines are the regions where $\theta_c \approx \theta_{c,SW}$. The bottom panel shows the ratio L/R . The thin white lines are the proton cyclotron frequency f_{cp} . The thick red and white line in the bottom panel are ten and six times the proton cyclotron frequency, respectively (see text).

frequencies, which is consistent with the presence of Doppler-shifted IC waves.

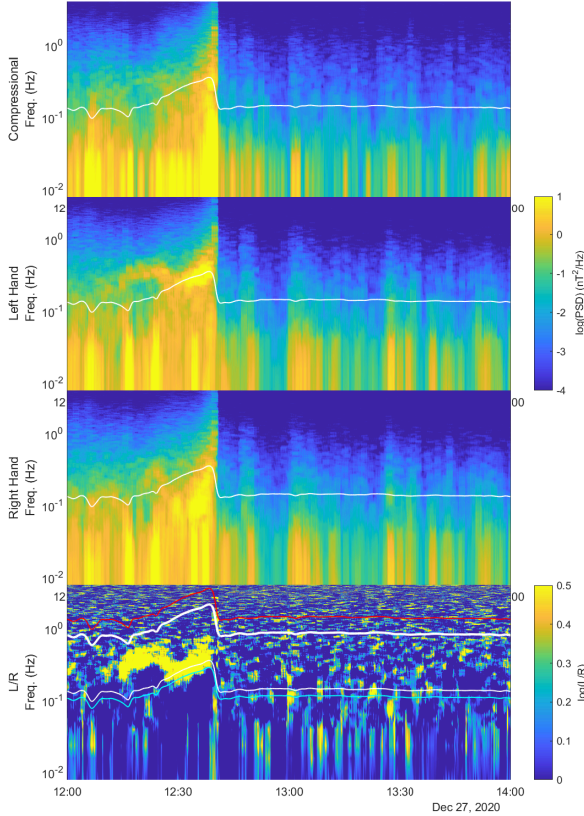
Assuming the IC waves propagate with the Alfvén velocity, $v_A \approx 30 \text{ km s}^{-1}$ (for $B_m = 8 \text{ nT}$ and $n = 40 \text{ cm}^{-3}$) and the plasma flow velocity in the magnetosheath is solar wind-like ($V_{SW} \approx 320 \text{ km s}^{-1}$), we estimate a Doppler-shift in frequency by a factor of ~ 10 . The red line in the bottom panel of Fig. 10 shows $10f_{cp}$, which seems to be the upper boundary of the patches up to $\sim 10:00$ UT, but is at higher frequencies than the peak of the wave power. The thick white line shows $6f_{cp}$, which seems to match the maxima rather well.

Using this assumption of Doppler-shifted cyclotron waves, an estimate can be made of the plasma flow velocity by inverting the Doppler shift equation, which then leads to $v_{MS} \approx 180 \text{ km s}^{-1}$. This would mean that the plasma in the magnetosheath has not yet been accelerated to solar wind speeds, even as far down the tail as $\sim 55 R_V$.

Close to Venus, between 10:00 and 13:00 UT, the strongest power lies at much lower frequencies than the red line, indicating a smaller Doppler shift, with the plasma flow velocity in the magnetosheath not yet accelerated up to V_{SW} . It should be noted that most of the strong left-hand power is occurring within the regions marked as having $\theta_c \approx \theta_{c,SW}$ (thus in the magnetosheath) and, interestingly, also at the location where the cone angle $\theta_c \approx 160^\circ$ (and thus in the tail proper) between $\sim 08:20$ and $\sim 08:45$ UT, after which there is a sudden decrease in the power in all components (Table 2).

Table 2. Ion cyclotron properties: the ellipticity and the propagation angle with respect to the background field.

Interval	Ellip.	Angle (°)
05:11:00–05:21:00	−0.75	5
08:35:00–08:44:00	−0.35	5
12:17:00–12:23:00	−0.57	20
13:31:00–13:36:00	−0.78	13
12:59:30–13:01:30	−0.38	20
13:22:45–13:23:45	−0.36	20

**Fig. 11.** Dynamical spectra of the compressional, left- and right-hand polarised field components around the bow shock. Same format as Fig. 10. The thin cyan line in the *bottom panel* shows the $0.8f_{cp}$ location.

4.1.2. Around the bow shock

The dynamic spectra of the magnetic field around the bow shock crossing can be seen in Fig. 11. Just downstream from the bow shock, there is a strong left-handed signature visible close to the local proton gyro frequency. Following this structure with the plasma flow, moving further into the magnetosheath (i.e. going back in time) the signature follows the proton cyclotron line, up to $\sim 12:30$ UT, after which it starts to deviate. The observed frequency increases from $\sim f_{cp}$ to $\sim 3f_{cp}$. This can be interpreted as locally produced IC waves by pick-up inside the bow shock, which are then Doppler shifted by the acceleration of the magnetosheath plasma flow (see, e.g., Spreiter et al. 1966; Spreiter & Stahara 1994).

In the solar wind, upstream of Venus’s bow shock, strong proton cyclotron wave power is expected, as was shown by Delva et al. (2008, 2009, 2015). Interestingly, in Fig. 11 there is little evidence for proton cyclotron waves in the upstream region.

These waves are usually between 0.8 and $1 f_{cp}$ (the white and cyan lines in the bottom panel). There are a few small enhancements in left-handed power at $\sim 13:00$, $\sim 13:25$ UT between the white and cyan line, which are interpreted as proton cyclotron waves and at $\sim 13:29$ UT below the cyan line, which might not, most likely, be associated with proton cyclotron waves.

Ion cyclotron waves just downstream of the quasi-perpendicular bow shock were also observed at Earth, for which the upstream plasma- $\beta < 0.5$ (Czaykowska et al. 2001); namely, a ‘low- β ’ shock. It was also shown that behind the bow shock the MM instability criterion was not at all, or only marginally, fulfilled. We estimate the solar wind plasma- β with $B_{SW} = 8$ nT, $N_{SW} = 20 \text{ cm}^{-3}$ and use a typical value of $T_{i,SW} = 13$ eV (Bader et al. 2019):

$$\beta_{SW} = \frac{Nk_B T}{B^2/2\mu_0} \approx 1.2. \quad (7)$$

In order to determine the plasma- β behind the bow shock the Rankine-Hugoniot relations (see, e.g., Baumjohann & Treumann 1996) are solved, with the numbers above as upstream input parameters, the average IMF magnetic field given in Sect. 3 and the bow shock normal calculated with Eq. (3). This results in $\beta_{MS} \approx 1.3$. Gary et al. (1993) shows that in the magnetosheath the temperature asymmetry T_{\perp}/T_{\parallel} must be $\sim 15\%$ larger for mirror mode generation than for ion cyclotron wave generation for $\beta_{MS} \approx 1.3$ to achieve the same growth rate.

4.2. Mirror modes and magnetic holes

MMs are often driven in high- β plasmas with a temperature anisotropy $T_{\perp} > T_{\parallel}$ (Gary et al. 1993). The instability criterion for a bi-Maxwellian distribution is (Southwood & Kivelson 1993):

$$R_{SK} = \frac{T_{i\perp}/T_{i\parallel}}{1 + 1/\beta_{i\perp}} > 1, \quad (8)$$

where

$$\beta_{i\perp} = \frac{n_i k_B T_{i\perp}}{B^2/2\mu_0}. \quad (9)$$

At Venus, and other planets, these structures are often observed behind the quasi-perpendicular bow shock, where the ions are heated mainly in the perpendicular to \mathbf{B} (Volwerk et al. 2008a,b, 2016). MMs consist of trains of magnetic field depressions combined with plasma density enhancements, balancing the total pressure. In the absence of adequate thermal plasma measurements, one can still identify these structures using magnetic field data only, as proposed by Lucek et al. (1999a,b), and later confirmed with plasma data by Rae et al. (2007).

The ‘Lucek’ method involves a MVA analysis within sliding windows of 10 s with a shift of 1 s obtaining the minimum variance \mathbf{n}_{min} and maximum variance \mathbf{n}_{max} directions, and determining a background magnetic field, \mathbf{B}_{bk} by low-pass filtering the data for periods longer than 0.5 min. MMs are characterised by two angles:

$$\angle(\mathbf{n}_{min}, \mathbf{B}_{bk}) \geq 80^\circ, \quad (10)$$

$$\angle(\mathbf{n}_{max}, \mathbf{B}_{bk}) \leq 20^\circ, \quad (11)$$

where the 20° derives from numerical simulations of MMs by Price et al. (1986), who actually find a maximum angle of 30° . Also, a limit is set to the ‘depth’ of the MM defined as:

$$\Delta|B|/|B| = (|B_{bk}| - |B_m|)/|B_{bk}| > 0.15. \quad (12)$$

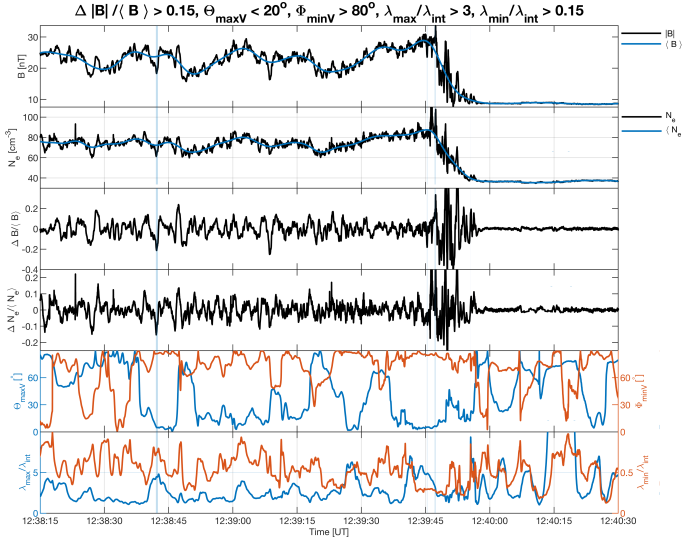


Fig. 12. Mirror mode identification. *From top to bottom:* magnetic field strength (black) and low-pass filtered background (blue); Electron density (black) and low-pass filtered background (blue); $\Delta B/B$; $\Delta N/N$; Angle between background magnetic field and minimum variance (red) and maximum variance (blue) direction; Eigenvalues ratios. Based on magnetic field-only categorisation the vertical blue bars are determined to be MMs. Including the electron density in the categorisation the MM identification is falsified as $\Delta B/B$ and $\Delta N/N$ are in phase.

With these conditions the blue-shaded areas in Fig. 12 are identified as candidate MMs, although it can be argued that by reducing the $\Delta|B|/|B|$ slightly, more structures that can be identified by eye as possible MMs are also found. However, it must be noted that the depth of the MMs is similar to that found by Volwerk et al. (2016).

However, taking into account that we have on hand an estimate of the electron density at sufficient resolution, another conclusion about these compressional magnetic field variations ought to be drawn. In contrast to true MMs, the magnetic field variation $\Delta B/B$ and the density variations $\Delta N/N$ are in phase. Therefore, these fluctuations may also be fast-mode or magnetosonic oscillations (see e.g., Shan et al. 2014).

Based on the conclusions in Sect. 4.1.2, namely, that there is strong IC wave activity behind the bow shock, the lack of MMs might not be particularly surprising. We argue that the plasma- β and the temperature asymmetry behind the bow shock favour the growth of IC waves instead of MMs.

However, the presence of MMs or magnetic holes (MHs) can be seen in the data further away from the bow shock, where those structures have had time to grow. Figure 13 shows an interval between 11:30:20 and 11:30:30 UT where the conditions in Eqs. (10)–(12) are satisfied and the magnetic field and density fluctuations are in anti-phase. Similarly, the interval 11:31:00–11:31:10 UT is also consistent with the presence of MMs or MHs. Here, the spacecraft is already at $X_{VSO} \approx -8 R_V$, far downstream of the bow shock.

5. Comparison with earlier missions

On 5 February 1974, Mariner 10, on its way to Mercury, flew along the length of Venus's magnetotail (wake), in an orbit in the X_R -plane similar to Solar Orbiter, however differing strongly in the Y - and Z -components. Lepping & Behannon (1978) studied the magnetic field data starting at a distance of $\sim 100 R_V$ from the planet. No evidence was found for a bow shock crossing

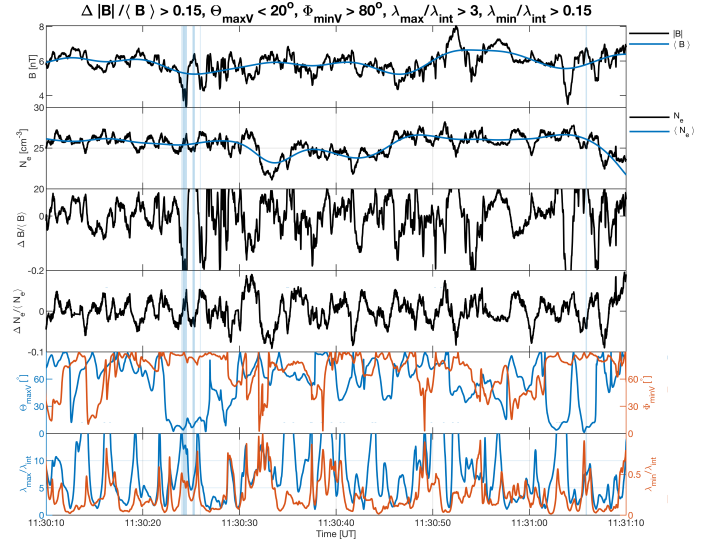


Fig. 13. Mirror mode identification based on B -field only measurements. Same format as Fig. 12. Because of the patent anti-correlation between plasma density and B_m -variations throughout the interval, the blue shaded intervals are most likely MMs or MHs.

entering the far tail. The authors did not observe a typical magnetotail structure (as compared to Earth). They found that, when the magnetic field direction and the spacecraft velocity vector aligned, the direction was not predominantly along X_{VSO} .

The data were categorised into three bins, quiet, disturbed, and mixed. It was found that the longitudinal (cylindrical) component of the field rotated clockwise, when the spacecraft crossed from a quiet to a disturbed region. This was interpreted as Mariner 10 entering into planetary tail field. This planetary field, however, had a significant Y -component for most crossings. The upstream conditions of the IMF are $F = 20\gamma$, $\phi \approx 360^\circ$, and $\theta \approx 0^\circ$ (Ness et al. 1974), indicating a mostly radial magnetic field. These crossings are reminiscent of the crossings by Solar Orbiter discussed above, where the spacecraft moves from the magnetosheath to the tail proper. There does not seem to be a similar variation in quiet or disturbed field in the Solar Orbiter data, where $\bar{F} \approx 7(8) \text{ nT}$ and $\text{rms}/\bar{F} \approx 1(1)$ for the ‘magnetosheath-quiet’ (‘magnetotail-disturbed’) intervals.

On its way to Jupiter, the Galileo spacecraft used a Venus gravitational assist, where the orbit skimmed the bow shock (see e.g., Kivelson et al. 1991). The magnetometer data were used to study the cross section of the far bow shock, which seemed to be smaller when it was aligned with the IMF direction compared to when it was perpendicular to the IMF.

Venus's near-tail region, at $|X| \lesssim 12 R_V$, was studied by Slavin et al. (2014) using Pioneer Venus data. Studying 12 passes through the central induced magnetotail (in the period 1981–1983) along Pioneer Venus's polar orbit, the authors found that the spacecraft was crossing the central current sheet multiple times during each crossing. From their figures, the quasi-period of the crossings is $\lesssim 10 \text{ min}$. The spacecraft moved from clearly defined, oppositely directed lobe fields and whether or not this can be considered magnetotail flapping is not addressed.

The main difference between the orbits studied by Slavin et al. (2014) and the Solar Orbiter Venus 1 flyby is the IMF direction and thereby the morphology of the induced magnetotail. For the Pioneer Venus orbits, the central current sheet was almost in the $X - Z$ -plane due to mainly B_Y -dominated IMF; whereas for Solar Orbiter, the IMF also had a

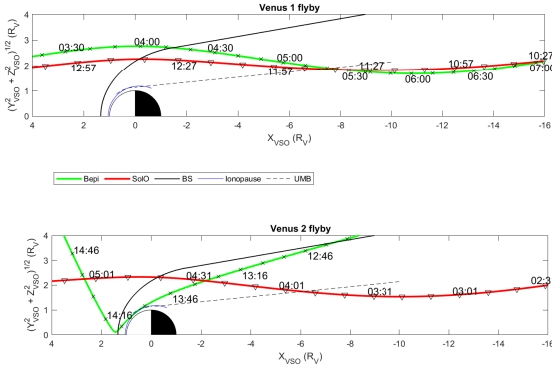


Fig. 14. First and second Venus flybys by Solar Orbiter and Bepi-Colombo in cylindrical VSO coordinates.

considerable B_z component, tilting the central plasma sheet away from the $X - Z$ -plane. In our approach, the magnetic field latitude, ϕ the cone-angle, θ_c were used for region identification, similarly to [Slavin et al. \(2014\)](#), as shown above.

6. Conclusions

The first Venus flyby by Solar Orbiter has delivered new insights into the large-scale structure of the induced Venusian magnetotail and magnetosheath, as well as the dynamical processes occurring within them. This flyby, along with the first Venus-flyby by BepiColombo, has allowed for the investigation of regions of Venus's magnetotail that have never been visited before. These unique data give insight in the extendedness of induced magnetosphere around and downstream of the planet.

The tail region downstream of the planet was shown to be rather active, with evidence of structures such as flux-ropes and reconnection sites, as well as cyclotron wave activity at smaller scales, close to the proton gyro radius. Interestingly, while a quasi-perpendicular bow shock is present, there is no enhanced mirror mode activity just downstream of the structure. Instead, we find evidence of strong wave activity at the local proton gyro frequency that is consistent with Doppler-shifted IC waves as well as evidence for fast-mode or magnetosonic waves. We interpret this Doppler-shift as arising from the accelerated plasma flow in the magnetosheath. Mirror mode or magnetic hole structures may instead have been identified far downstream of the shock. Upstream of the bow shock, in the solar wind, there is only little evidence of expected proton cyclotron waves.

Fortunately, there are several more Venus flybys by Solar Orbiter to come, which will allow us investigate the tail further. The next one will be on 9 August 2021, immediately followed by BepiColombo's flyby on 10 August. Here, the synergy of both spacecraft being near Venus at the same time can be used, such that one can act as a solar wind monitor whilst the other is passing through the induced magnetosphere. Figure 14 shows the orbits of both spacecraft, for the Venus 1 and 2 flybys in cylindrical coordinates. Solar Orbiter has a similar orbit, whereas Bepi-Colombo enters more deeply into the sub-solar magnetosphere. In further flybys of Venus by Solar Orbiter, the spacecraft will move much closer to the planet, also arriving at the planet from different directions.

Unfortunately, this flyby was hampered by the lack of the Solar Wind Analyser (SWA, [Owen et al. 2020](#)) data, which would have provided high-resolution ion and electron distributions. These data would have helped, for instance, in establishing the magnetosheath plasma flow velocity and the proton temperature anisotropies, which can be determined from the

velocity distribution functions. This first Venus flyby has already shown that there is still plenty to investigate and to understand about the induced magnetosphere of Venus.

Acknowledgements. Solar Orbiter is a mission of international cooperation between ESA and NASA, operated by ESA. The RPW instrument has been designed and funded by CNES, CNRS, the Paris Observatory, The Swedish National Space Agency, ESA-PRODEX and all the participating institutes. The work by CSW is supported by the Austrian Science Fund (FWF) under project P32035-N36. M.B.S. acknowledges support by PRODEX Experiment Arrangement (PEA) No. C 4000106749 “RPW Phase C/D – Solar Orbiter”. D.S. work is financially supported by the Austrian Research Promotion Agency (FFG) ASAP MERMAG-4 under contract 865967. L.D.W. is supported by STFC consolidated grant ST/S000364/1 to Imperial College London. R.C.A. and G.C.H. are supported under NASA contract NNN06AA01C and thank NASA headquarters and the NASA/GSFC Solar Orbiter project office for their continuing support. L.B. and STEP are funded by Germany's DLR grant No. 500T2002. Solar Orbiter magnetometer operations are funded by the UK Space Agency (grant ST/T001062/1). T.H. is supported by STFC grant ST/S000364/1. The work by Y.V.K. is supported by the Swedish National Space Agency grant 20/136.

References

- Allen, R. C., Mason, G. M., Ho, G. C., et al. 2021, *A&A*, **656**, L2 (SO Cruise Phase SI)
- Anselmi, A., & Scoon, G. E. N. 2001, *Planet. Space Sci.*, **49**, 1409
- Bader, A., Stenberg Wieser, G., André, M., et al. 2019, *J. Geophys. Res.*, **124**, 3312
- Bale, S. D., Kasper, J. C., Howes, G. G., et al. 2009, *Phys. Rev. Lett.*, **103**, 211101
- Baumjohann, W., & Treumann, R. A. 1996, *Basic Space Plasma Physics* (London, UK: Imperial College Press)
- Benkhoff, J., Casteren, J., Hayakawa, H., et al. 2010, *Planet. Space Sci.*, **58**, 2
- Bertucci, C., Duru, F., Edberg, N., et al. 2011, *Space Sci. Rev.*, **162**, 113
- Bowen, T. A., Bale, S. D., Bandyopadhyay, R., et al. 2021, *Geophys. Res. Lett.*, **48**, e90783
- Czaykowska, A., Bauer, T. M., Treumann, R. A., & Baumjohann, W. 2001, *Ann. Geophys.*, **19**, 275
- Delva, M., Zhang, T. L., Volwerk, M., Vörös, Z., & Pope, S. A. 2008, *Geophys. Res. Lett.*, **113**, E00B06
- Delva, M., Volwerk, M., Mazelle, C., et al. 2009, *Geophys. Res. Lett.*, **36**, L01203
- Delva, M., Bertucci, C., Volwerk, M., et al. 2015, *J. Geophys. Res.*, **120**, 344
- Delva, M., Volwerk, M., Jarvinen, R., & Bertucci, C. 2017, *J. Geophys. Res.*, **122**, 10396
- Dimmock, A. P., Khotyaintsev, Yu. V., Lalti, A., et al. 2021, *A&A*, submitted (SO Cruise Phase SI)
- Dubinin, E., Fraenz, M., Fedorov, A., et al. 2011, *Space Sci. Rev.*, **162**, 173
- Dubinin, E., Fraenz, M., Woch, J., et al. 2013, *Planet. Space Sci.*, **87**, 19
- Fox, N. J., Velli, M. C., Bale, S. D., et al. 2016, *Space Sci. Rev.*, **204**, 7
- Fränz, M., Echer, E., Marquez de Souza, A., Dubinin, E., & Zhang, T. L. 2017, *Planet. Space Sci.*, **146**, 55
- Futaana, Y., Stenberg Wieser, G., Barabash, S., & Luhmann, J. G. 2017, *Space Sci. Rev.*, **212**, 1543
- Gary, S. P. 1992, *J. Geophys. Res.*, **97**, 8519
- Gary, S. P., Fuselier, S. A., & Anderson, B. J. 1993, *J. Geophys. Res.*, **98**, 1481
- Goodrich, K. A., Bonnell, J. W., Curry, S., et al. 2021, *Geophys. Res. Lett.*, **48**, e90329
- Hadid, L. Z., Edberg, N. J. T., Chust, T., et al. 2021, *A&A*, **656**, A18 (SO Cruise Phase SI)
- Hellinger, P., Travnicek, P., Kasper, J. C., & Lazarus, A. J. 2006, *Geophys. Res. Lett.*, **33**, L09101
- Horbury, T. S., O'Brien, H., Carrasco Blazquez, I., et al. 2020, *A&A*, **642**, A9
- Khotyaintsev, Yu. V., Graham, D. B., Vaivads, A., et al. 2021, *A&A*, **656**, A19 (SO Cruise Phase SI)
- Kivelson, M. G., Kennel, C. F., McPherron, R. L., et al. 1991, *Science*, **253**, 1518
- Lepping, R. P., & Behannon, K. W. 1978, *J. Geophys. Res.*, **83**, 3709
- Lucek, E. A., Dunlop, M. W., Balogh, A., et al. 1999a, *Ann. Geophys.*, **17**, 1560
- Lucek, E. A., Dunlop, M. W., Balogh, A., et al. 1999b, *Geophys. Res. Lett.*, **26**, 2159
- Luhmann, J. G. 1986, *Space Sci. Rev.*, **44**, 241
- Maksimovic, M., Bale, S. D., Chust, T., et al. *A&A*, **642**, 2020
- Malaspina, D. M., Goodrich, K., Livi, R., et al. 2020, *Geophys. Res. Lett.*, **47**, e90115
- Martinez, C., Boesswetter, A., Fränz, M., et al. 2009a, *J. Geophys. Res.*, **114**, E00B30

- Martinecz, C., Boesswetter, A., Fränz, M., et al. 2009b, *J. Geophys. Res.*, **114**, E00B98
- Matteini, L., Landi, S., Hellinger, P., et al. 2007, *Geophys. Res. Lett.*, **34**, L20105
- Mazelle, C., & Neubauer, F. M. 1993, *Geophys. Res. Lett.*, **20**, 153
- Müller, D., Marsden, R. G., St. Cyr, O. C., Gilbert, H. R., & The Solar Orbiter Team 2013, *Sol. Phys.*, **285**, 25
- Müller, D., St. Cyr, O. C., Zouganelis, I., et al. 2020, *A&A*, **642**, A1
- Ness, N. F., Behannon, K. W., Lepping, R. P., Whang, Y. C., & Schatten, K. H. 1974, *Science*, **185**, 151
- Owen, C. J., Bruno, R., Livi, S., et al. 2020, *A&A*, **642**, A16
- Phillips, J. L., & McComas, D. J. 1991, *Space Sci. Rev.*, **55**, 1
- Phillips, J. L., & Russell, C. T. 1987, *J. Geophys. Res.*, **92**, 2253
- Price, C. P., Swift, W., & Lee, L.-C. 1986, *J. Geophys. Res.*, **91**, 101
- Rae, I. J., Mann, I. R., Watt, C. E. J., Kistler, L. M., & Baumjohann, W. 2007, *J. Geophys. Res.*, **112**, A11203
- Rodríguez-Pacheco, J., Wimmer-Schweingruber, R. F., Mason, G. M., et al. 2020, *A&A*, **642**, A7
- Rong, J. Z., Barabash, S., Stenberg, G., et al. 2015, *J. Geophys. Res.*, **120**, 5593
- Russell, C. T., Luhmann, J. G., Elphic, R. C., & Scarf, F. L. 1981, *Geophys. Res. Lett.*, **8**, 843
- Saunders, M. A., & Russell, C. T. 1986, *J. Geophys. Res.*, **91**, 5589
- Schmid, D., Volwerk, M., Nakamura, R., Baumjohann, W., & Heyn, M. 2011, *Ann. Geophys.*, **29**, 1537
- Schwartz, S. J. 1998, in *Analysis Methods for Multi-Spacecraft Data*, eds. G. Paschmann, & P. Daly (Noordwijk: ESA), 249
- Shan, L. C., Lu, Q., Wu, M., et al. 2014, *J. Geophys. Res.*, **119**, 237
- Slavin, J. A., Intrilligator, D. S., & Smith, E. J. 2014, *J. Geophys. Res.*, **94**, 2383
- Sonnerup, B. U., & Scheible, M. 1998, in *Analysis Methods for Multi-Spacecraft Data*, eds. G. Paschmann, & P. Daly (Noordwijk: ESA), 185
- Southwood, D. J., & Kivelson, M. G. 1993, *J. Geophys. Res.*, **98**, 9181
- Spreiter, J. R., & Stahara, S. S. 1994, *Adv. Space Res.*, **14**, 5
- Spreiter, J., Summers, A., & Alksne, A. 1966, *Planet. Space Sci.*, **14**, 223
- Treumann, R., & Baumjohann, W. 1996, *Advanced Space Plasma Physics* (London, UK: Imperial College Press)
- Van Allen, J. A., Krimigis, S. M., Frank, L. A., & Armstrong, T. P. 1967, *Science*, **158**, 1673
- Volwerk, M., Zhang, T. L., Delva, M., et al. 2008a, *Geophys. Res. Lett.*, **35**, L12204
- Volwerk, M., Zhang, T. L., Delva, M., et al. 2008b, *J. Geophys. Res.*, **113**, E00B16
- Volwerk, M., Delva, M., Futaana, Y., et al. 2009, *Ann. Geophys.*, **27**, 2321
- Volwerk, M., Delva, M., Futaana, Y., et al. 2010, *Ann. Geophys.*, **28**, 1877
- Volwerk, M., Schmid, D., Tsurutani, B. T., et al. 2016, *Ann. Geophys.*, **34**, 1099
- Volwerk, M., Sánchez-Cano, B., Heyner, D., et al. 2021, *Ann. Geophys.*, **39**, 811
- Vörös, Z., Zhang, T. L., Leaner, M. P., et al. 2008a, *J. Geophys. Res.*, **113**, E00B21
- Vörös, Z., Zhang, T., Leubner, M. P., et al. 2008b, *Geophys. Res. Lett.*, **35**, L11102
- Woodham, L. D., Wicks, R. T., Verscharen, D., & Owen, C. J. 2018, *ApJ*, **856**, 49
- Woodham, L. D., Wicks, R. T., Verscharen, D., et al. 2019, *ApJ*, **884**, L53
- Zhang, T. L., Delva, M., Baumjohann, W., et al. 2008a, *Planet. Space Sci.*, **56**, 790
- Zhang, T. L., Delva, M., Baumjohann, W., et al. 2008b, *Planet. Space Sci.*, **56**, 785
- Zhang, T. L., Baumjohann, W., Du, J., et al. 2010, *Geophys. Res. Lett.*, **37**, L14202